

# High-yield engineering of modified divacancies in 4H-SiC via oxygen-ion implantation

Qi-Cheng Hu,<sup>1,2,3,4</sup> Ji-Yang Zhou,<sup>1,2,3</sup> Shuo Ren,<sup>1,2,3</sup> Zhen-Xuan He,<sup>1,2,3,4</sup> Zhi-He Hao,<sup>1,2,3</sup> Rui-Jian Liang,<sup>1,2,3</sup> Wu-Xi Lin,<sup>1,2,3,4</sup> Adam Gali,<sup>5,6,7</sup> Jin-Shi Xu,<sup>1,2,3,4,\*</sup> Chuan-Feng Li,<sup>1,2,3,4,†</sup> and Guang-Can Guo<sup>1,2,3,4</sup>

<sup>1</sup>Laboratory of Quantum Information, University of Science and Technology of China, Hefei, Anhui 230026, China

<sup>2</sup>Anhui Province Key Laboratory of Quantum Network,

University of Science and Technology of China, Hefei, Anhui 230026, China

<sup>3</sup>CAS Center For Excellence in Quantum Information and Quantum Physics,

University of Science and Technology of China, Hefei, Anhui 230026, China

<sup>4</sup>Hefei National Laboratory, University of Science and Technology of China, Hefei, Anhui 230088, China

<sup>5</sup>HUN-REN Wigner Research Centre for Physics,

Institute for Solid State Physics and Optics, P.O. Box 49, H-1525 Budapest, Hungary

<sup>6</sup>Department of Atomic Physics, Institute of Physics,

Budapest University of Technology and Economics,

Műgyetem rakpart 3., H-1111 Budapest, Hungary

<sup>7</sup>MTA-WFK "Lendület" Momentum Semiconductor Nanostructures Research Group, P.O. Box 49, H-1525 Budapest, Hungary

Modified divacancies in the 4H polytype of silicon carbide (SiC) exhibit enhanced charge stability and spin addressability at room temperature, making them highly attractive for quantum applications. However, their low formation yield, both at the single-defect and ensemble levels, has limited further progress. Here, we demonstrate a controllable and efficient method for generating modified divacancy color centers in 4H-SiC via oxygen-ion implantation. Based on their distinct optical signatures and spin-resonance characteristics, we experimentally resolve four types of modified divacancies. Remarkably, single modified divacancies constitute above 90% of the total defect population and exhibit superior optical properties and spin coherence compared with defects created through conventional carbon- or nitrogen-ion implantation. We characterize the zero-phonon lines of these modified divacancies and reveal a distinct temperature-dependent behavior in the spin-readout contrast. By systematically optimizing the implantation dose and annealing temperature, we further achieve high-density ensembles and observe clear Rabi-oscillation beating patterns associated with different orientations of basal-type defects. These results establish oxygen-ion implantation as a powerful and versatile approach to engineering high-quality spin-active defects in SiC, representing a significant advance toward scalable solid-state quantum technologies. Furthermore, our findings provide key insights into the atomic configurations of modified divacancies in 4H-SiC.

## INTRODUCTION

Solid-state spin qubits in silicon carbide (SiC) have emerged as promising building blocks for scalable quantum technologies [1–17]. Among these, the neutral divacancy is an ideal quantum platform due to its bright emission, long spin coherence, and high readout fidelity [1, 2, 4, 6]. Experimental and theoretical studies have identified PL1–PL4 as carbon–silicon divacancy complexes, which correspond to adjacent missing atoms at cubic (*k*) and hexagonal (*h*) lattice sites [18–21].

Beyond these well-understood divacancies, another group of defects, labeled PL5–PL8, exhibits zero-field splitting (ZFS) and zero-phonon line (ZPL) characteristics similar to PL1–PL4 and has thus been tentatively classified as modified divacancies [1, 2, 4, 6, 18–22]. Among them, single PL5 and PL6 centers display strong room-temperature photoluminescence, stable charge states, and pronounced spin contrast [4, 5]. However, their atomic configurations remain unclear, and their low formation yield limits device applications. In addition, the absence of a distinct ZPL for PL7 [18] fur-

ther obscures the microscopic origin of this family of defects.

Early models attributed PL5–PL7 to stacking-fault regions [23–25], but subsequent experiments have challenged this hypothesis. Specifically, irradiation-induced stacking faults in *n*-type 4H-SiC failed to generate PL5–PL7 centers [24]. These inconsistencies have motivated the search for alternative atomic configurations.

Recent theoretical investigations have identified oxygen-related defects in SiC as a distinct family of color centers [26, 27]. Based on this insight, *ab initio* calculations have proposed that neutral oxygen-substituted silicon vacancies at the *hk* and *hh* sites may account for PL5 and PL6 [28]. These models successfully reproduce the experimentally observed ZFS and ZPL values and predict symmetry axes consistent with experimental observations. However, no systematic experimental investigation of spin defects in 4H-SiC generated by oxygen-ion implantation had been reported. Here, we present a detailed investigation of the color centers generated by oxygen-ion implantation in 4H-SiC. At a dose of  $1 \times 10^8 \text{ cm}^{-2}$ , four dominant color centers are observed. Two of them exhibit optical and spin characteristics consistent with the previously identified PL5 and PL6 defects, while the other two—designated PL7' and PL8'—display distinct properties. PL7' is likely related

\* Email: jsxu@ustc.edu.cn

† Email: cfl@ustc.edu.cn

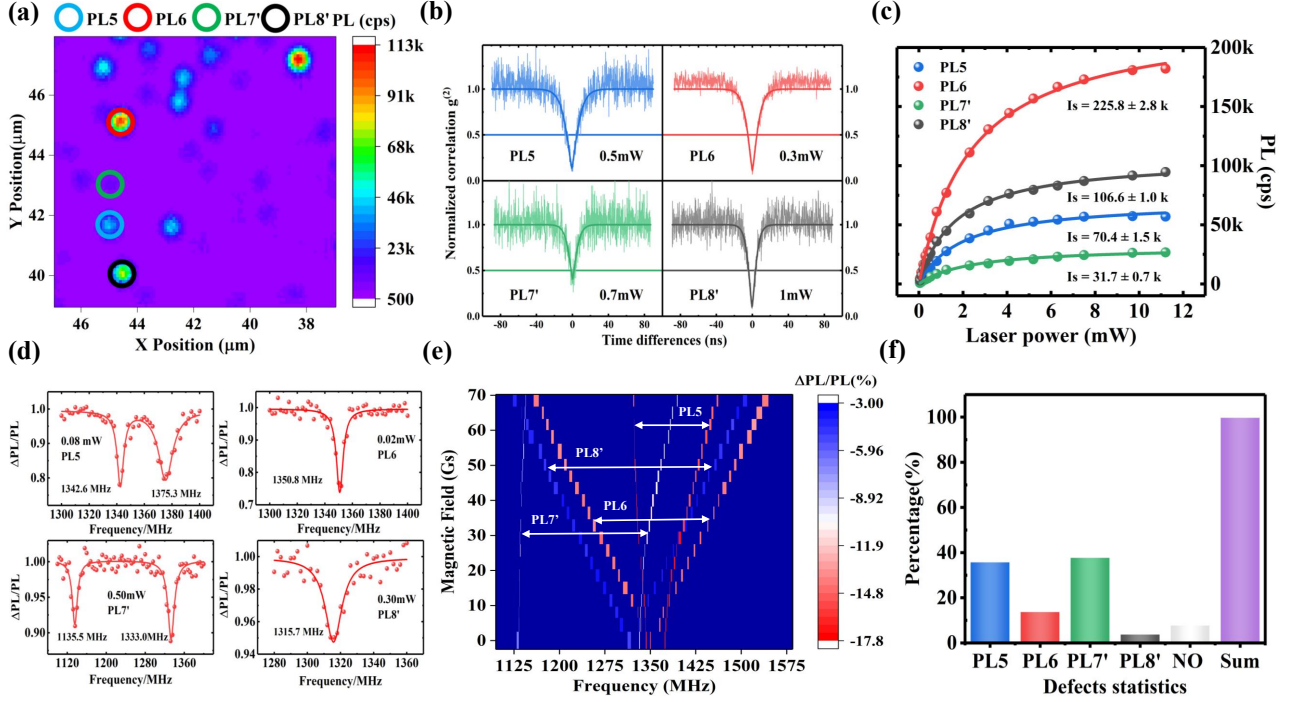


FIG. 1. Single modified divacancies in oxygen ion-implanted samples. (a) Photoluminescence (PL) map of a  $10 \times 10 \mu\text{m}^2$  region under 914 nm excitation with 2 mW laser power. The blue, red, green, and black circles indicate the locations of PL5, PL6, PL7', and PL8' color centers, respectively. (b) Second-order autocorrelation functions  $g^2(\tau)$  of PL5–PL8' obtained under high excitation power, shown without background subtraction. (c) Saturation curves of fluorescence count rates measured for PL5–PL8'. (d) Zero-field optically detected magnetic resonance (ODMR) spectra of PL5–PL8', recorded under different laser powers and -20 dB microwave power. (e) Magnetic-field-dependent ODMR responses of PL5–PL8' at 0.8 mW. (f) Statistical distribution of color center types among 149 randomly selected emitters at room temperature.

to the previously reported basal-like PL7, sharing several spectral features, whereas PL8' represents a newly identified *c*-axis-like defect; its zero-field splitting (ZFS) and zero-phonon line (ZPL) values agree well with theoretical predictions for oxygen-vacancy complexes [28]. Notably, the generation yield of these single modified divacancies is exceptionally high—together they account for more than 90% of the total defect population.

Room-temperature spin coherence measurements reveal significantly prolonged  $T_2$  times for PL5 and PL6 compared with carbon- and nitrogen-implanted samples [4, 6, 15, 19]. Temperature-dependent ODMR measurements reveal distinct contrast evolutions among the four signals: the contrast of the PL7' resonance decreases at low temperature, that of PL8' increases, the PL6 contrast remains almost unchanged, and the PL5 resonances become mixed—one branch maintains its contrast while the other shows a noticeable reduction. Ensemble measurements further reveal that high-dose oxygen implantation suppresses the PL1–PL4 emissions while enhancing the PL5–PL8' features, resulting in the appearance of clear Rabi oscillation beating patterns associated with the basal defects at room temperature.

These results establish oxygen-ion implantation as a controllable and efficient route for engineering modi-

fied divacancies with superior optical and spin coherence properties. This work paves the way for their applications in quantum sensing and communication and provides valuable insights into their atomic origins.

## RESULTS

### A. Preparation of single modified divacancies

The formation yield of modified divacancies is inherently low for carbon and nitrogen implantation, often requiring high doses to obtain isolated defects. However, excessive doses increase lattice damage and degrade the signal-to-noise ratio. To address this trade-off, we employed oxygen-ion implantation at a reduced dose of  $1 \times 10^8 \text{ cm}^{-2}$  to generate single modified divacancies. Details of the sample preparation are provided in the *Methods* section.

Fig. 1a shows a  $10 \times 10 \mu\text{m}^2$  photoluminescence (PL) map recorded under 2.0 mW excitation. Four types of spin-active color centers—PL5, PL6, PL7', and PL8'—are identified and highlighted by colored circles. These emitters exhibit high signal-to-noise ratios even without any post-annealing surface treatment. Details on the comparison of carbon, nitrogen, and oxygen ion implantation are provided in Supplementary Information

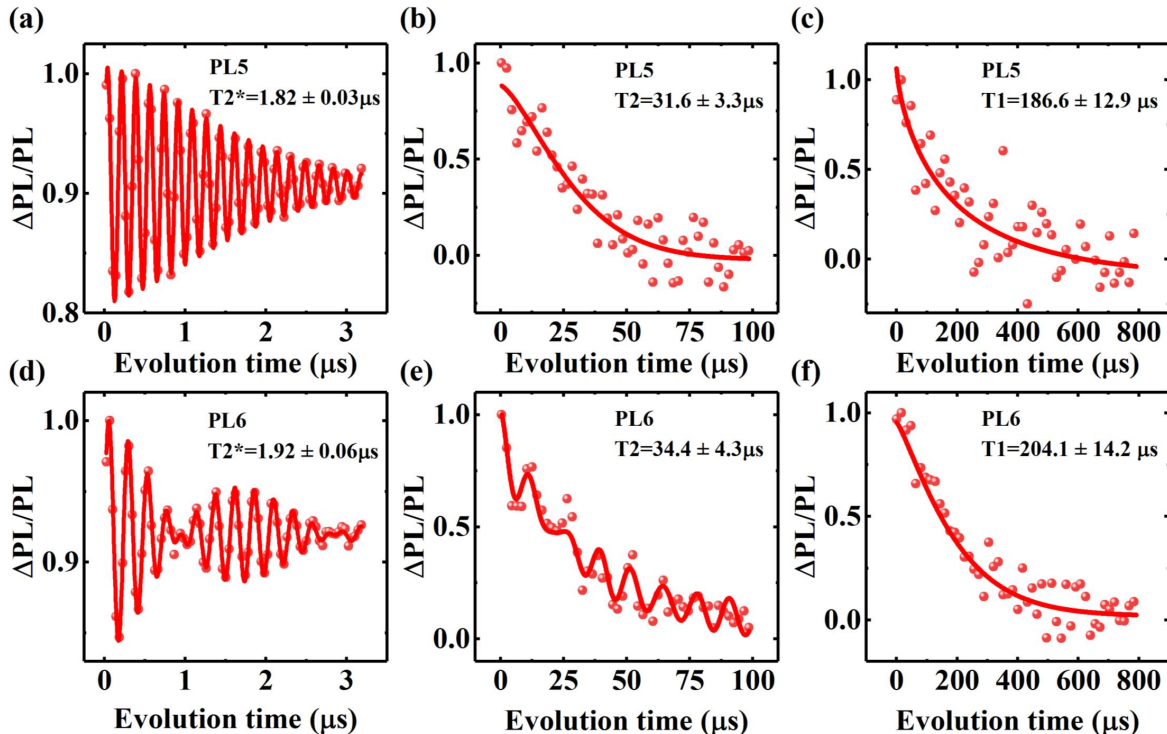


FIG. 2. Spin coherent control of single PL5 and PL6 centers. (a) Ramsey measurement of the inhomogeneous dephasing time ( $T_2^*$ ) for PL5 at 0 G. (b) Spin coherence time ( $T_2$ ) measurement of the left branch of PL5. (c) Spin-lattice relaxation time ( $T_1$ ) measurement of PL5 at 0 G. (d) Ramsey measurement of the inhomogeneous dephasing time ( $T_2^*$ ) for PL6 at 0 G. (e) Spin coherence time ( $T_2$ ) measurement of the left branch of PL6 at 180 G. (f) Spin-lattice relaxation time ( $T_1$ ) measurement of PL6 at 180 G.

A.

The single-photon nature of the emitters was verified by measuring the second-order autocorrelation function  $g^{(2)}(\tau)$  as a function of time delay  $\tau$  (Fig. 1b). The experimental raw data under low excitation power were analyzed by fitting to the following model [4, 29]:  $g^{(2)}(\tau) = 1 - (1 + a)e^{-|\tau-\tau_0|/t_1} + be^{-|\tau-\tau_0|/t_2}$ , where  $\tau_0$  represents the time delay at zero point, and  $t_1, t_2, a, b$  are fitting parameters. For all four defects,  $g^{(2)}(0)$  values remain below 0.5 without background subtraction, confirming single-photon emission. High-power  $g^{(2)}(\tau)$  measurements are provided in Supplementary Information B.

The fluorescence saturation curves in Fig. 1c yield saturation count rates and powers of  $70.4 \pm 1.5$  kcps and  $1.93 \pm 0.13$  mW for PL5,  $225.8 \pm 2.8$  kcps and  $2.36 \pm 0.09$  mW for PL6,  $31.7 \pm 0.7$  kcps and  $2.33 \pm 0.14$  mW for PL7', and  $106.6 \pm 1.0$  kcps and  $1.66 \pm 0.05$  mW for PL8'. Among them, PL6 is the brightest single emitter at room temperature—consistent with results from carbon-ion implantation [4]—whereas PL7' is the weakest, being more than seven times dimmer than PL6.

Continuous-wave optically detected magnetic resonance (ODMR) spectra of individual centers are presented in Fig. 1d. PL5 exhibits two zero-field resonances at 1342.6 and 1375.3 MHz with 20% contrast;

the extracted zero-field splitting parameters are  $D = 1358.9$  MHz and  $E = 16.6$  MHz. PL6 shows a single sharp resonance at 1350.8 MHz with 25% contrast, consistent with previous reports [1, 4, 19, 22, 30]. PL7' displays a double-resonance feature at 1135.5 and 1333.0 MHz, with  $D = 1234.2$  MHz and  $E = 98.8$  MHz. While ensemble studies previously attributed the 1135 MHz peak to PL3, no single-defect evidence had been reported [22]. Our results suggest that the previously reported PL7 center may correspond to this double-resonant structure. PL8' exhibits a single resonance at 1315.7 MHz with a lower  $\sim 5\%$  contrast, different from PL1 (1323.5 MHz) [4], hinting at a new type of room-temperature spin qubit.

The magnetic-field-dependent ODMR spectra (Fig. 1e) confirm that PL5 and PL7' are basal-plane oriented, while PL6 and PL8' align along the c-axis. PL5, PL6, and PL7' display pronounced contrasts, whereas PL8' retains a lower ( $\sim 5\%$ ) room-temperature contrast. Statistical analysis of 149 emitters (Fig. 1f) reveals that 92% correspond to modified divacancy centers. Detailed statistical results are provided in Supplementary Information C. These observations strongly indicate that oxygen incorporation plays a crucial role in transforming divacancy configurations.

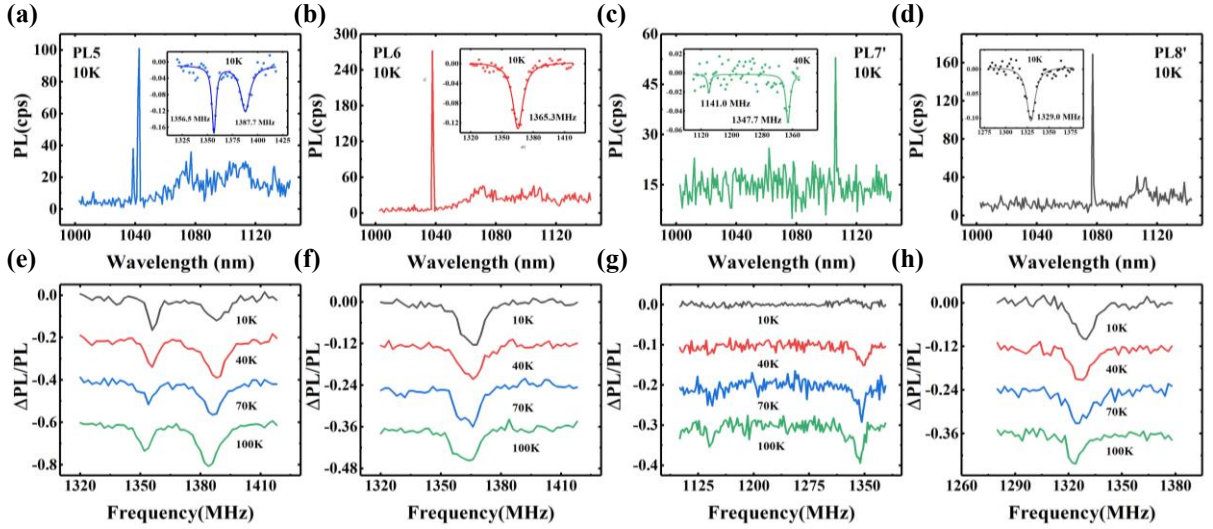


FIG. 3. Zero-phonon line (ZPL) and zero-field splitting (ZFS) of single modified divacancy defects. (a-d) Measured zero-phonon line (ZPL) and zero-field splitting (ZFS) of a single emitter at cryogenic temperature. (e-h) Temperature-dependent ODMR spectra of PL5–PL8’.

### B. Coherent control of single modified divacancies

Spin coherence properties are central to the applicability of color centers in quantum technologies. The modified divacancies represent a typical three-level system ( $S = 1$ ), whose spin Hamiltonian under an external magnetic field can be expressed as:

$$\mathcal{H} = D \left( S_z^2 - \frac{S(S+1)}{3} \right) + E(S_x^2 - S_y^2) + g\mu_B \mathbf{B} \cdot \mathbf{S}, \quad (1)$$

where  $D$  and  $E$  are the zero-field splitting parameters,  $g_e$  is the electron  $g$ -factor,  $\mu_B$  is the Bohr magneton,  $\mathbf{B}$  is the applied magnetic field, and  $\mathbf{S}$  is the spin operator. We characterized PL5, PL6, PL7’, and PL8’ in terms of their Ramsey inhomogeneous dephasing time ( $T_2^*$ ), spin coherence time ( $T_2$ ), and spin–lattice relaxation time ( $T_1$ ), all measured under a relatively high optical power of 0.8 mW.

The basal-oriented PL5 color center hosts  $m_s = \pm 1$  energy levels that exist in mixed states. With the left branch designated as the  $|+\rangle = 1/\sqrt{2}(|1\rangle + |-1\rangle)$  state, optical polarization initializes the system to the  $|0\rangle$  state, enabling coherent manipulation from  $|0\rangle$  to  $|+\rangle$  via microwave excitation. While, the c-axis oriented PL6 color center exhibits degeneracy lifting of the  $m_s = \pm 1$  levels under an applied magnetic field along the c-axis. With the left branch defined as the  $|1\rangle$  state, we performed coherent measurements on the  $|0\rangle$  to  $|1\rangle$  transition.

For PL5 (Fig. 2a–2c), we obtained  $T_2^* = 1.82 \pm 0.03 \mu\text{s}$ ,  $T_2 = 31.6 \pm 3.3 \mu\text{s}$ , and  $T_1 = 186.6 \pm 12.9 \mu\text{s}$  at zero magnetic field. These values surpass those of carbon- and nitrogen-implanted defects [4, 6]. PL6 (Fig. 2d–2f) exhibited even longer coherence, with  $T_2^* = 1.92 \pm 0.06 \mu\text{s}$ ,  $T_2 = 33.4 \pm 4.3 \mu\text{s}$ , and  $T_1 = 204.1 \pm 14.2 \mu\text{s}$  at 180 G.

In the Ramsey fringes of PL6, we observed characteristic modulations arising from weakly coupled  $^{29}\text{Si}$  nuclear spins [4].

The natural abundance of  $^{29}\text{Si}$  (4.7%) and  $^{13}\text{C}$  (1.1%) provides a dense nuclear spin reservoir, making these centers promising candidates for hybrid electron–nuclear quantum registers. The coherence data for PL7’ and PL8’ are provided in Supplementary Information D. Owing to their excellent optical and spin properties, particularly the controllable implantation depth, these single modified defects are highly suitable for quantum sensing [31]. Stopping and Range of Ions in Matter (SRIM) simulations for the implantation process are presented in Supplementary Information E. The application of shallow single PL6 centers for near-surface magnetic sensing is demonstrated in Supplementary Information F.

### C. Low-temperature properties of single modified divacancies

Cryogenic ODMR and PL spectroscopy (Fig. 3a–3d) were performed on the same single centers tracked during cooling. PL5 exhibits a ZPL at 1042.2 nm and zero-field splitting (ZFS) of 1356.5 and 1387.7 MHz; PL6 shows a ZPL at 1037.8 nm and a ZFS of 1365.3 MHz, consistent with earlier reports [1, 4, 19, 22]. A weak emission near the PL5 ZPL appears in most samples, reminiscent of the V1/V1’ doublet in silicon vacancies [32].

PL7’ shows a ZPL at 1106.2 nm, close to that of PL3 (1108 nm) [1, 4, 19, 22]. The identical ZPL and the temperature dependence of its ODMR contrast suggest that PL7’ likely corresponds to the previously reported PL3a [18, 22, 33], which might in fact be identical to the basal-like PL7 defect. This spectral proximity could ex-

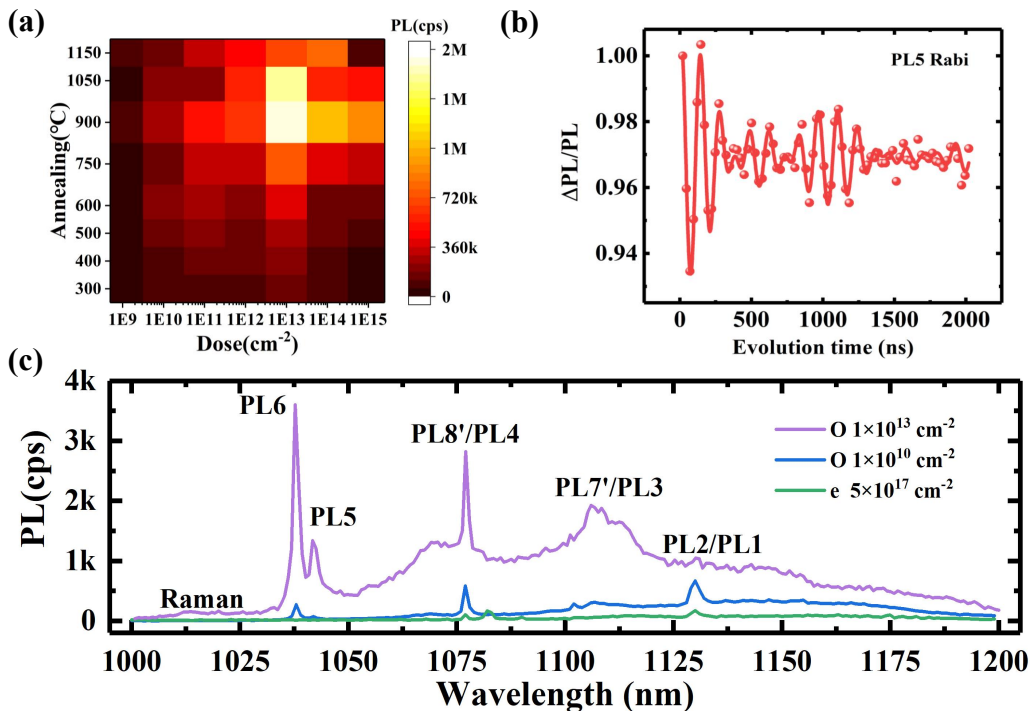


FIG. 4. Optical and spin properties of ensemble samples. (a) Optimization of implantation dose and annealing temperature for oxygen-implanted ensembles. (b) Rabi oscillation measurements of PL5 centers with the characteristic beating patterns. (c) Low-temperature ZPL spectra of ensembles with oxygen ion implantation of different doses, as well as electron irradiation.

plain why the PL7' line was previously unresolved at low temperatures. PL8' exhibits a ZPL at 1077.1 nm, near that of PL4 (1078 nm), but displays distinct ODMR features with *c*-axis orientation. These weak-contrast centers were likely overlooked in earlier ensemble measurements [19, 22, 30, 33].

Temperature-dependent ODMR spectra reveal contrasting behaviors among the centers. For PL5 (Fig. 3c), the right branch of the ODMR signal weakens markedly below 10 K, while the left branch remains stable. PL6 shows minimal change from 100 K to 10 K (Fig. 3d). In contrast, the ODMR contrast of PL7' vanishes near 10 K (Fig. 3e). Conversely, PL8' exhibits increasing ODMR contrast upon cooling, reaching nearly twice its room-temperature value at 10 K (Fig. 3f). These trends highlight PL8' as a promising spin qubit candidate for cryogenic quantum applications. The distinct temperature-dependent behaviors further confirm the differences among these defects and provide a pathway for investigating temperature-dependent intersystem crossing processes.

The measured ZPLs of 1.1947, 1.1899, 1.1513, and 1.1208 eV for PL5, PL6, PL7', and PL8', respectively, agree well with the theoretically calculated values of 1.212, 1.205, 1.163, and 1.131 eV for the *hk*, *hh*, *kh*, and *kk* oxygen-silicon-vacancy complexes [28]. This agreement further supports the hypothesis that oxygen is closely involved in the formation of these defects. Key parameters of the different centers are summarized in

Supplementary Table 1.

#### D. High-concentration ensembles

We next optimized ensemble samples by systematically tuning the oxygen implantation dose and annealing temperature. The corresponding PL intensities are shown in Fig. 4a. Under 0.1 mW excitation, samples implanted with  $1 \times 10^{13} \text{ cm}^{-2}$  oxygen ions and annealed at 900°C for 0.5 h in vacuum exhibited PL intensities exceeding 1.7 Mcps—significantly higher than those in previously reported ensemble samples [19, 30]. The estimated defect concentration is approximately  $1 \times 10^{16} \text{ cm}^{-3}$  [14, 30], which will help advance the development of quantum sensing technologies for high-pressure, magnetic field, and other applications [10, 14, 30]. The silicon vacancies in the same samples were optimized in Supplementary Information G.

We further found that the nitrogen concentration strongly affected the generation efficiency of the modified divacancies. When the nitrogen concentration increased from below  $1 \times 10^{14} \text{ cm}^{-3}$  to  $1 \times 10^{19} \text{ cm}^{-3}$ , the PL intensity at the optimal implantation dose and annealing temperature decreased by about a factor of ten. A detailed investigation of the role of nitrogen concentration is presented in Supplementary Information H.

Rabi oscillation measurements of PL5 centers (Fig. 4b) revealed characteristic beating patterns,

consistent with previous reports using substrate samples [1]. For the PL5 Rabi oscillations, we employed a triple-cosine exponentially decaying function for fitting:  $f(t) = a + b \cdot \exp[-(\frac{t}{\tau})^n] \cdot [\cos(2\pi\Omega_1 t + \phi_1) \cdot \cos(2\pi\Omega_2 t + \phi_2) \cdot \cos(2\pi\Omega_3 t + \phi_3)]$ , which indicates the superposition of multiple distinct Rabi frequencies under a single microwave driving field, suggesting complex coherent dynamics in the system. This behavior arises from the anisotropic nature of PL5 centers, which possess three basal orientations within the lattice. Each orientation experiences a distinct microwave driving strength due to the vectorial nature of the microwave field, resulting in orientation-dependent Rabi frequencies ( $\Omega_1$ ,  $\Omega_2$  and  $\Omega_3$ ) that manifest as observable beatings in the time-domain signal. The parameters  $a$ ,  $b$ ,  $\tau$ ,  $\phi_1$ ,  $\phi_2$  and  $\phi_3$  are fitting parameters. The optical and spin characteristics of the PL5 and PL6 ensembles, presented in Supplementary Information I and J, are consistent with those observed in the corresponding single-defect cases.

Comparative ensemble studies using different doses of oxygen ion implantation, as well as electron irradiation under the same annealing conditions, are summarized in Fig. 4c. Electron-irradiated samples showed negligible ZPL emissions from modified divacancies. Increasing the oxygen dose from  $1 \times 10^{10} \text{ cm}^{-2}$  to  $1 \times 10^{13} \text{ cm}^{-2}$  suppressed PL1 and PL2 entirely, while PL6 becomes the dominant ZPL contributor. This trend indicates that oxygen ions promote a higher conversion yield of modified divacancies.

## CONCLUSION AND DISCUSSION

In summary, we have demonstrated that oxygen-ion implantation offers an effective and controllable approach to generating modified divacancy color centers in 4H-SiC. Four distinct spin-active centers—PL5, PL6, PL7', and PL8'—were successfully created and systematically characterized in terms of their optical and spin properties, including zero-phonon lines (ZPLs), zero-field splittings (ZFSs), magnetic-field dependence, and temperature-dependent behavior. Our results suggest that PL7' likely corresponds to the previously reported PL7, and we have identified PL8' as a new single-spin defect. The measured zero-phonon lines (ZPLs), zero-field splittings (ZFSs), and spin coherence times agree well with theoretical predictions for oxygen-related complexes [26–28, 34], providing strong evidence that oxygen incorporation is crucial in stably generating these defects.

Direct verification of the oxygen-vacancy structure via hyperfine interactions with the oxygen nuclear spin (e.g., using the  $^{17}\text{O}$  isotope with  $I = 5/2$ ) remains challenging [35]. In our experiments with samples implanted with 70%  $^{17}\text{O}$ , no discernible differences were observed compared with  $^{16}\text{O}$ -implanted samples. This indicates that the four modified divacancies may not correspond to simple oxygen-vacancy complexes but instead involve more complex structures, or that oxygen plays a catalytic role in their formation—a possibility that warrants further

investigation.

The controllable generation of single modified divacancies in SiC holds significant potential for single-spin quantum sensing [31]. In this work, shallow PL6 centers were successfully applied to near-surface magnetic-field sensing. Additionally, the production of high-concentration, high-quality ensembles and their demonstrated performance in magnetic sensing mark a substantial step toward practical solid-state quantum technology. The superior optical and spin properties of these defects make them promising candidates for room-temperature quantum sensing, scalable quantum networks, and spin-photon interfaces.

## METHODS

**Sample preparation** An *n*-type single-crystal 4H-SiC epitaxial layer with a thickness of approximately  $11 \mu\text{m}$  was grown on a  $4^\circ$  off-axis 4H-SiC substrate. The nitrogen doping concentration was below  $1 \times 10^{14} \text{ cm}^{-3}$ .

For single-defect preparation, oxygen ions were implanted at a dose of  $1 \times 10^8 \text{ cm}^{-2}$ , followed by annealing in an  $\text{Ar}_2$  atmosphere at  $1050^\circ\text{C}$ . For ensemble-defect preparation, samples were implanted with doses ranging from  $1 \times 10^9$  to  $1 \times 10^{15} \text{ cm}^{-2}$  and subsequently annealed under identical vacuum conditions at temperatures of 300, 400, 500, 600, 750, 900, 1050, and  $1150^\circ\text{C}$  for 0.5 hours each.

**Experimental setups** Optical measurements were performed using a home-built confocal microscopy system. A 914 nm laser served as the excitation source, coupled into the setup through a 950 nm short-pass filter and a 980 nm dichroic mirror, and focused onto the sample using an objective lens with a numerical aperture of 0.85. Photoluminescence was collected through a 1000 nm long-pass filter and coupled into a 1060 nm single-mode fiber.

For low-temperature measurements, the sample was mounted in a Montana Instruments cryostat equipped with an Autocube positioning stage. Room-temperature imaging was performed using a piezoelectric scanner, whereas low-temperature imaging employed a two-axis galvo scanning system with silver-coated mirrors (Thorlabs, GVS012). Photon detection was carried out using a superconducting nanowire single-photon detector (Photon Technology Co.).

Laser and microwave pulse sequences were modulated by an acousto-optic modulator (AOM; Gooch & Housego) and microwave switches (Mini-Circuits, ZASWA-2-50DRA+), both synchronized by a pulse generator (SpinCore, PBESR-PRO-500-PCI). Microwave (MW) signals were generated by a signal generator (Mini-Circuits, SSG-6000-RC), amplified by a power amplifier (Mini-Circuits, ZHL-25W-272+), and delivered to the sample through a  $20 \mu\text{m}$ -diameter copper wire.

A Time Tagger device was employed for second-order correlation function ( $g^{(2)}(\tau)$ ) measurements. Spectra were recorded using a custom-built single-photon spec-

trometer consisting of a Newport high-precision rotation stage and a diffraction grating (600 lines/mm, blaze wavelength 1000 nm, blaze angle 17.46°).

## ACKNOWLEDGEMENT

This work was supported by the Quantum Science and Technology-National Science and Technology Major Project (No. 2021ZD0301400 and No. 2021ZD0301200), National Natural Science Foundation of China (No. 92365205 and No. W2411001), and USTC Major Frontier Research Program (No. LS2030000002). This work was partially performed at the University of Science and Technology of China Center for Micro and Nanoscale Research and Fabrication.

## AUTHOR CONTRIBUTIONS STATEMENT

J.-S. X. and C.-F. L. conceived the experiments. Q.-C. H. built the experimental setup and carried out the measurements with assistance from J.-Y. Z., S.-R., Z.-X. H., Z.-H. H., R.-J. L., and W.-X. L. A. G. provided the theoretical analysis and suggested the comparison using oxygen-isotope-implanted samples. Q.-C. H. and J.-S. X. analyzed the data and wrote the manuscript, with input from all co-authors. J.-S. X., C.-F. L., and G.-C. G. supervised the project. All authors discussed the results.

## COMPETING INTERESTS STATEMENT

The authors declare no competing interests.

- 
- [1] Koehl, W. F., Buckley, B. B., Heremans, F. J., Calusine, G. & Awschalom, D. D. Room temperature coherent control of defect spin qubits in silicon carbide. *Nature* **479**, 84–87 (2011).
- [2] Christle, D. J., Falk, A. L., Andrich, P., Klimov, P. V., Hassan, J. U., Son, N. T., Janzén, E., Ohshima, T. & Awschalom, D. D. Isolated electron spins in silicon carbide with millisecond coherence times. *Nat. Mater.* **14**, 160–163 (2015).
- [3] Widmann, M., Lee, S.-Y., Rendler, T., Son, N. T., Fedder, H., Paik, S., Yang, L.-P., Zhao, N., Yang, S., Booker, I., et al. Coherent control of single spins in silicon carbide at room temperature. *Nat. Mater.* **14**, 164–168 (2015).
- [4] Li, Q., Wang, J.-F., Yan, F.-F., Zhou, J.-Y., Wang, H.-F., Liu, H., Guo, L.-P., Zhou, X., Gali, A., Liu, Z.-H., et al. Room-temperature coherent manipulation of single-spin qubits in silicon carbide with a high readout contrast. *Nat. Sci. Rev.* **9**, nwab122 (2022).
- [5] He, Z.-X., Zhou, J.-Y., Li, Q., Lin, W.-X., Liang, R.-J., Wang, J.-F., Wen, X.-L., Hao, Z.-H., Liu, W., Ren, S., Li, H., You, L.-X., Zhang, R.-J., Zhang, F., Tang, J.-S., Xu, J.-S., Li, C.-F. & Guo, G.-C. Robust single modified divacancy color centers in 4H-SiC under resonant excitation. *Nat. Commun.* **15**, 10146 (2024).
- [6] Yan, F.-F., Yi, A.-L., Wang, J.-F., Li, Q., Yu, P., Zhang, J.-X., Gali, A., Wang, Y., Xu, J.-S., Ou, X., et al. Room-temperature coherent control of implanted defect spins in silicon carbide. *npj Quantum Inf.* **6**, 38 (2020).
- [7] Lukin, D. M., Dory, C., Guidry, M. A., Yang, K. Y., Mishra, S. D., Trivedi, R., Radulaski, M., Sun, S., Ver-cruysse, D., Ahn, G. H., et al. 4H-silicon-carbide-on-insulator for integrated quantum and nonlinear photonics. *Nat. Photonics* **14**, 330–334 (2020).
- [8] Babin, C., Stöhr, R., Morioka, N., Linkewitz, T., Steidl, T., Wörnle, R., Liu, D., Hesselmeier, E., Vorobyov, V., Denisenko, A., et al. Fabrication and nanophotonic waveguide integration of silicon carbide colour centres with preserved spin-optical coherence. *Nat. Mater.* **21**, 67–73 (2022).
- [9] Bourassa, A., Anderson, C. P., Miao, K. C., Onizhuk, M., Ma, H., Crook, A. L., Abe, H., Ul-Hassan, J., Ohshima, T., Son, N. T., et al. Entanglement and control of single nuclear spins in isotopically engineered silicon carbide. *Nat. Mater.* **19**, 1319–1325 (2020).
- [10] Wang, J.-F., Liu, L., Liu, X.-D., Li, Q., Cui, J.-M., Zhou, D.-F., Zhou, J.-Y., Wei, Y., Xu, H.-A., Xu, W., et al. Magnetic detection under high pressures using designed silicon vacancy centres in silicon carbide. *Nat. Mater.* **22**, 489–494 (2023).
- [11] Wang, J.-F., Yan, F.-F., Li, Q., Liu, Z.-H., Liu, H., Guo, G.-P., Guo, L.-P., Zhou, X., Cui, J.-M., Wang, J., et al. Coherent control of nitrogen-vacancy center spins in silicon carbide at room temperature. *Phys. Rev. Lett.* **124**, 223601 (2020).
- [12] Jiang, Z., Cai, H., Cernansky, R., Liu, X. & Gao, W. Quantum sensing of radio-frequency signal with NV centers in SiC. *Sci. Adv.* **9**, eadg2080 (2023).
- [13] Wang, J.-F., Yan, F.-F., Li, Q., Liu, Z.-H., Cui, J.-M., Liu, Z.-D., Gali, A., Xu, J.-S., Li, C.-F. & Guo, G.-C. Robust coherent control of solid-state spin qubits using anti-Stokes excitation. *Nat. Commun.* **12**, 3223 (2021).
- [14] Abraham, J. B. S., Gutgsell, C., Todorovski, D., Sperling, S., Epstein, J. E., Tien-Street, B. S., Sweeney, T. M., Wathen, J. J., Pogue, E. A., Brereton, P. G., et al. Nanotesla magnetometry with the silicon vacancy in silicon carbide. *Phys. Rev. Appl.* **15**, 064022 (2021).
- [15] Bracher, D. O., Zhang, X. & Hu, E. L. Selective Purcell enhancement of two closely linked zero-phonon transitions of a silicon carbide color center. *Proc. Natl. Acad. Sci. USA* **114**, 4060–4065 (2017).
- [16] Nagy, R., Niethammer, M., Widmann, M., Chen, Y.-C., Udvarhelyi, P., Bonato, C., Hassan, J. U., Karhu, R., Ivanov, I. G., Son, N. T., et al. High-fidelity spin and optical control of single silicon-vacancy centres in silicon carbide. *Nat. Commun.* **10**, 1954 (2019).
- [17] Niethammer, M., Widmann, M., Lee, S.-Y., Stenberg, P., Kordina, O., Ohshima, T., Son, N. T., Janzén, E. & Wrachtrup, J. Vector magnetometry using silicon vacancies in 4H-SiC under ambient conditions. *Phys. Rev. Appl.* **6**, 034001 (2016).
- [18] Magnusson, B., Son, N. T., Csóré, A., Gällström, A., Ohshima, T., Gali, A. & Ivanov, I. G. Excitation properties of the divacancy in 4H-SiC. *Phys. Rev. B* **98**, 195202 (2018).
- [19] Falk, A. L., Buckley, B. B., Calusine, G., Koehl, W. F., Dobrovitski, V. V., Politi, A., Zorman, C. A., Feng, P. X.-L. & Awschalom, D. D. Polytype control of spin qubits in silicon carbide. *Nat. Commun.* **4**, 1819 (2013).

- [20] Gordon, L., Janotti, A. & Van de Walle, C. G. Defects as qubits in 3C- and 4H-SiC. *Phys. Rev. B* **92**, 045208 (2015).
- [21] Davidsson, J., Ivády, V., Armiento, R., Son, N. T., Gali, A. & Abrikosov, I. A. First principles predictions of magneto-optical data for semiconductor point defect identification: the case of divacancy defects in 4H-SiC. *New J. Phys.* **20**, 023035 (2018).
- [22] Shafizadeh, D., Son, N. T., Abrikosov, I. A. & Ivanov, I. G. Evolution of the optically detected magnetic resonance spectra of divacancies in 4H-SiC from liquid-helium to room temperature. *Phys. Rev. B* **111**, 165201 (2025).
- [23] Ivády, V., Davidsson, J., Deegan, N., Falk, A. L., Klimov, P. V., Whiteley, S. J., Hruszkewycz, S. O., Holt, M. V., Heremans, F. J., Son, N. T., et al. Stabilization of point-defect spin qubits by quantum wells. *Nat. Commun.* **10**, 5607 (2019).
- [24] Son, N. T., Anderson, C. P., Bourassa, A., Miao, K. C., Babin, C., Widmann, M., Niethammer, M., Ul Hassan, J., Morioka, N., Ivanov, I. G., et al. Developing silicon carbide for quantum spintronics. *Appl. Phys. Lett.* **116**, 190501 (2020).
- [25] Castelletto, S. Silicon carbide single-photon sources: challenges and prospects. *Mater. Quantum Technol.* **1**, 023001 (2021).
- [26] Iwamoto, S., Shimura, T., Watanabe, H. & Kobayashi, T. Oxygen-related defects in 4H-SiC from first principles. *Appl. Phys. Express* **17**, 051008 (2024).
- [27] Kobayashi, T., Shimura, T. & Watanabe, H. Oxygen-vacancy defect in 4H-SiC as a near-infrared emitter: An ab initio study. *J. Appl. Phys.* **134**, 143102 (2023).
- [28] Bai, R., Liu, D., Chen, S. & Wu, Y.-N. Origin of the unidentified color centers in 4H-SiC from first principles. *Phys. Rev. B* **111**, 014106 (2025).
- [29] Castelletto, S., Johnson, B. C., Ivády, V., Stavrias, N., Umeda, T., Gali, A. & Ohshima, T. A silicon carbide room-temperature single-photon source. *Nat. Mater.* **13**, 151–156 (2014).
- [30] Wang, J.-F., Cui, J.-M., Yan, F.-F., Li, Q., Cheng, Z.-D., Liu, Z.-H., Lin, Z.-H., Xu, J.-S., Li, C.-F. & Guo, G.-C. Optimization of power broadening in optically detected magnetic resonance of defect spins in silicon carbide. *Phys. Rev. B* **101**, 064102 (2020).
- [31] Li, P., Zhou, J.-Y., Li, S., Udvarhelyi, P., Xu, J.-S., Li, C.-F., Huang, B., Guo, G.-C. & Gali, A. Non-invasive bioinert room-temperature quantum sensor from silicon carbide qubits. *Nat. Mater.* <https://doi.org/10.1038/s41563-025-02382-9>, 1 (2025).
- [32] Nagy, R., Widmann, M., Niethammer, M., Dasari, D. B. R., Gerhardt, I., Soykal, Ö. O., Radulaski, M., Ohshima, T., Vučković, J., Son, N. T., et al. Quantum properties of dichroic silicon vacancies in silicon carbide. *Phys. Rev. Appl.* **9**, 034022 (2018).
- [33] Son, N. T., Shafizadeh, D., Ohshima, T. & Ivanov, I. G. Modified divacancies in 4H-SiC. *J. Appl. Phys.* **132**, 025701 (2022).
- [34] Zhao, X., Liu, M. & Duan, C.-K. Towards identifying the PL6 center in SiC: From first-principles screening to hyperfine validation of competing defect candidates. *Phys. Rev. Mater.* **9**, 116204 (2025).
- [35] Pezzagna, S., Diziain, S., Martelock, H., Neugebauer, P., Michaelis, J., Lühmann, T. & Meijer, J. Polymorphs of 17O-Implanted ST1 Spin Centers in Diamond and Spectroscopy of Strongly Coupled <sup>13</sup>C Nuclear Spins. *ACS Photon.* **11**, 1969–1980 (2024).